Exp Fluids manuscript No.
(will be inserted by the editor)

The effect of active grid initial conditions on high Reynolds number turbulence

R. J. Hearst · P. Lavoie

the date of receipt and acceptance should be inserted later

Abstract The most expansive active grid parametric study to date is conducted in order to ascertain the relative importance of the various grid parameters. It is identified that the three most important parameters are the Rossby number, Ro, the grid Reynolds number, Re_M, and the wing geometry. For $Ro > 50$, an asymptotic state in turbulence intensity is reached where increasing Ro further does not change the turbulence intensity while other parameters continue to vary. Three wing geometries are used: solid square wings, solid circular wings, and square wings with holes. It is shown that the wings with the greatest blockage produce the highest turbulence intensities and Re_λ, but that parameters such as the Kolmogorov, Taylor and integral scales are not significantly influenced by wing geometry. Finally, it is demonstrated that for several different sets of initial conditions that produce the same Re_λ, the spectra are collapsed everywhere but at the largest scales. This result suggests that regardless of the very different origins of the turbulence, the shape of the spectra at high wavenumbers is dependent only on Re_λ when normalized by Kolmogorov variables, hence demonstrating a degree of independence from the initial conditions.

1 Introduction

Our traditional understanding of turbulence is derived from the Richardson-Kolmogorov cascade that describes energy being passed down from the large scales to successively smaller scales until it is dissipated as heat. According to this description, if the local Reynolds number, Re_λ, is sufficiently high, the turbulence can exhibit a universal state over a subset of scales that are independent of the initial generating conditions. However, traditional grid turbulence experiments have demonstrated that there is a dependence of the produced turbulence on the initial conditions at low to moderate Reynolds numbers (Comte-Bellot and Corrsin, 1966; Lavoie et al., 2007). As such, the question of the relative importance of the initial conditions on the flow at high Reynolds numbers remains open.

Mydlarski and Warhaft (1996) constructed an active grid, based on the design of Makita (1991), to investigate high Re_λ turbulence in an endeavour to approach the limit where the classical high Re_λ physics may be observed. This style of active grid consists of a series of 'wings' mounted to rods that are actuated in a random pattern by stepper motors. The grid constructed by Mydlarski and Warhaft (1996) was an $8M \times 8M$ array, where M is a mesh length, and it was placed in a $0.4\,\mathrm{m} \times 0.4\,\mathrm{m}$ wind tunnel. When comparing the turbulence produced by their grid to Kolmogorov's (1941) $k^{-5/3}$ law, they found that even $Re_\lambda \approx 500$ was not sufficient to satisfy high Reynolds number conditions. In a follow-up study, Mydlarski and Warhaft (1998) constructed a larger $8M \times 8M$ grid for a $0.9\ \mathrm{m} \times 0.9\ \mathrm{m}$ wind tunnel. Again, they found that for the increased $Re_\lambda \approx 730$, $k^{-5/3}$ behaviour was not reached for the velocity spectra, however, they did observe $k^{-5/3}$ scaling for the scalar (temperature) spectrum, suggesting that the scalar spectrum reaches a possible universal state earlier than the velocity fluctuations.

Since this seminal work by Mydlarski and Warhaft (1996, 1998), a number of other groups have designed active grids in an attempt to either reach high Re_λ or to be able to control the characteristics of the generated turbulence. The most extensive parametric study of active grid generated turbulence to date was performed by Larssen and Devenport (2011) who placed more emphasis on the variability of the produced turbulence than on high Re_λ turbulence theory. Larssen and Devenport (2011) placed a $10M \times 10M$ active grid in

R. J. Hearst · P. Lavoie
Institute for Aerospace Studies, University of Toronto
Toronto, ON M3H 5T6, Canada
Tel.: +1-416-667-7716
Fax.: +1-416-667-7799
E-mail: lavoie@utias.utoronto.ca

the contraction of a 1.83 m × 1.83 m wind tunnel. By placing the grid in the contraction they were able to achieve global isotropy ratios near unity as originally demonstrated by Comte-Bellot and Corrsin (1966) with passive grids. In their study, Larssen and Devenport (2011) produced turbulence with $101 \leq Re_\lambda \leq 1362$, $2\% \leq u'/U \leq 12\%$, and $0.24 \leq L_{ux}/M \leq 3.19$, representing some of the highest Re_λ and largest scale turbulence produced by a grid experiment to date. They found that the two parameters that were most important for characterizing the active grid-generated turbulence were the grid Reynolds number, $Re_M = UM/\nu$, and the Rossby number, $Ro = U/\Omega M$ (where Ω is the mean rotational velocity of the grid agitator wings).

A recent advancement by Bodenschatz et al. (2014) has introduced a 129 degree-of-freedom, $9M \times 9M$ active grid in a 1.5 m × 1.5 m wind tunnel. Each wing of this grid is mechanically independent, unlike previous grids where all wings along a single axis were rigidly connected and moved together. With this new apparatus, Bewley et al. (2013) showed that with certain correlated motions of adjacent wings they were able to control the size of the large scale motion in the produced turbulence.

Several other Makita-style active grids have been designed and built for a variety of applications. Poorte and Biesheuvel (2002) used an active grid in water to investigate the motion of spherical bubbles in the grid wake. Kang et al. (2003) used an active grid to extend the work of Comte-Bellot and Corrsin (1971) to higher Reynolds numbers in order to compare the results with large eddy simulations. Cekli and van de Water (2010), Cal et al. (2010) and Knebel et al. (2011) have designed active grids to simulate atmospheric shear layers. Sytsma and Ukeiley (2013) investigated the effect of turbulence on lift generated by a flat plate, and Sharp et al. (2009) studied the impact of free-stream turbulence on a turbulent boundary layer. Finally, Thormann and Meneveau (2014) used fractal pattern wings to investigate how the turbulent kinetic energy decayed in the wake of such initial conditions.

The present study uses a novel variant of the Makita (1991) active grid to address questions concerning high Re_λ physics and to gain a better understanding of the active grid parameter space. In particular, we produce high Re_λ turbulence at a given Re_λ with different initial conditions in order to assess if the turbulence shows any signs of 'remembering' how it was produced. The parametric study of Larssen and Devenport (2011) is also extended here in order to more fully understand the influence of active grid parameters on the produced turbulence.

The paper is organized as follows. Section 2 discusses the active grid design and experimental setup. Section 3 presents the results of the parametric study identifying what grid parameters have the greatest influence over the produced turbulence. Section 4 then compares test cases from section 3 where similar Re_λ were produced with different initial conditions in order to assess if the turbulence spectra collapse for a given Re_λ, or if the differing initial conditions are able to produce turbulence with the same Re_λ, but different spectral shapes. Finally, section 5 presents the concluding arguments.

2 Experimental Setup

2.1 Active grid design

The active grid utilizes a double-mesh design of steel rods with diameter 6.35 mm. The meshes are separated by 40 mm in the streamwise direction. Wings are mounted to the forward and aft meshes in an alternating pattern such that half the wings are on one mesh and the remaining wings are on the other, see Fig. 1. With this setup, adjacent wings are never in the same plane along a single rod. Therefore, the motion of adjacent wings can be decoupled, creating a more random spatial sequence than attainable by traditional active grids. The grid consists of 20 horizontal bars and 30 vertical bars, oriented as two layers of a 10×15 mesh, with a mesh length of $M = 80$ mm. The only grid with greater variability is that of Bodenschatz et al. (2014), although the present grid has nearly twice the number of bars, which reduces the confinement effect of the tunnel size on the turbulence. Low friction cylindrical supports (diameter 12.7 mm) hold the various meshes of the grid apart, and help maintain overall rigidity. While these supports were not required at every mesh length, they were placed at every junction in order to create a homogeneous background mesh. The 50 grid bars were actuated by Applied Motion Products STM23S-3RN integrated stepper motors. The motors were controlled via two RS-485 serial ports through a PC. Each motor was sent a top-hat distribution of: rotational velocity, $\Omega \pm \omega$; rotational period, $T \pm t$; and rotational acceleration, $A \pm \alpha$ (where in the formulation $B \pm \beta$, B is the mean of the quantity and $\pm\beta$ represents the bounds of the random variation). The grid rods were rotated at rotational rates ranging from 0 to 20 Hz. The acceleration was varied between 0 and 250 Hz/s. The average period of rotation was varied between 2 and 8 seconds. One of the limiting factors in the operation of the grid was that in order to prevent data collisions in the serial communication, a minimum time delay of 40 ms had to be enforced between communications to the grid.

Mounted to the rotating grid rods were 254 wings. Two wing geometries were tested: square wings (55 mm × 55 mm), and circular wings (diameter 55 mm). Holes of diameter 20 mm were cut out of the square wings, and tests were conducted both with the holes open and with them covered by aluminum tape (as depicted in Fig. 1(b)). Circular wings have not previously been investigated in the literature and were introduced here to remove the sharp corners of the square

wings with the intention of potentially avoiding streamwise vortices from the edges that could induce long streamwise correlations. Schematics of the wing geometries are shown in Fig. 2.

The active grid was operated in one of 8 modes. In fully random (FR) mode, every rod received a unique random signal, and there was no deliberate correlation between the motion of the grid rods. In classical (CL) mode, rod pairs mounted immediately upstream/downstream of one another on the forward and aft meshes were deliberately sent the same signal so that the grid behaved as if there was only one mesh, simulating a traditional active grid. These two base modes, FR and CL, were also used to create a series of grid control sequences with varying degrees of correlation between grid rods. For instance, in 2FR mode, two adjacent rods on one of the meshes received the same signal. The CL mode that corresponds to 2FR is 4CL, where two adjacent rods on the forward mesh received the same signal, and the two rods on the aft mesh immediately downstream of the first two rods also received that the same signal, i.e., a total of 4 rods received the same signal and moved in unison. All operational modes used in this study are summarized in Table 1.

2.2 Instrumentation

All experiments were performed in the low-speed, recirculating wind tunnel at the University of Toronto Institute for Aerospace Studies. The wind tunnel has a hexagonal test-section that is 1.2 m wide, 0.8 m tall and 5 m long. The hexagonal corners are adjustable so that an approximately zero pressure gradient may be achieved along the test-section length. Tests were conducted with mean velocities between 3 m/s and 16 m/s. The background turbulence intensity in the wind tunnel does not exceed 0.06% in this velocity range.

Measurements were performed with a constant temperature hot-wire anemometer built at the University of Newcastle (Miller et al., 1987). Both single-wires and X-wires were employed. Single-wires (SW1, SW2, and SW3) with different sensing lengths were used in order to verify that the results were not a consequence of limited spatial resolution. Wire dimensions are given in Table 2, where ℓ is the sensing length and d is the wire diameter. The single-wires were made in-house with tungsten wire. The region outside of the sensing length was coated with copper. The tolerance on wire sensing length was ±0.1 mm. Two X-wires (XW1 and XW2) with different sensing lengths were used. XW1 was an Auspex A55P51 probe. XW2 was made in-house on the same prongs as XW1, but with smaller wire. The mean Kolmogorov microscale ($\eta = \nu^{3/4}/\langle\epsilon\rangle^{1/4}$) over all measurements was ~ 0.2 mm, and typical probe resolutions are provided in Table 2 based on this value. The hot-wires were

Table 2: Hot-wire probe dimensions.

	SW1, SW2	SW3	XW1	XW2	
ℓ	1.1	0.6	1.2	0.6	mm
d	5.0	2.5	5.0	2.5	μm
ℓ/η	5.5	3.0	6.0	3.0	

operated with an overheat ratio of 1.6 and an analog cut-off filter at $f_c = 9.2$ kHz. The sampling frequency was set to $f_s = 2f_c + 1$ kHz. Data were acquired with a 16-bit National Instruments PCI-6259 card. Samples were taken for 4 minutes or longer to ensure ±1% statistical convergence of $\langle q^2\rangle = \langle u^2\rangle + 2\langle v^2\rangle$ using the 95% confidence interval (Benedict and Gould, 1996); it was verified that $\langle v^2\rangle \approx \langle w^2\rangle$ in the present flow by rotating the X-wire 90°. Single-wires were calibrated with a 4$^{\text{th}}$-order polynomial fit to 10 velocities. The X-wire was calibrated over 10 velocities and 7 angles using the look-up table approach discussed by Burattini and Antonia (2005). All calibrations were performed *in situ* with the grid set to its fully open position (15% blockage with 1.7% turbulence intensity at $x/M = 30$).

The principal setup employed SW1 and XW1 separated by 10 mm, and mounted to a 4 degree-of-freedom (3 translational and 1 rotational) traverse system. The home position of the system was at the centre of the tunnel cross-section. This setup was used to perform both parametric study measurements at the centre of the tunnel cross-section and to perform transverse planar measurements for the assessment of flow homogeneity. The secondary setup featured two single-wires, SW2 mounted to a fixed stand at $y/H = +0.14$ ($H = 400$ mm is the tunnel half-height), and SW1 mounted to a vertical traverse system. These probes were sequentially separated by known amounts in order to determine the transverse correlation, $B_{uu}(r_y) = \langle u(x)\,u(x+r_y)\rangle$, at various separations, r_y, along the y-axis. This correlation was then used to compute the transverse integral length scale, L_{uy}, from

$$L_{\alpha\beta} = \frac{1}{\langle\alpha^2\rangle}\int_0^{r_{\beta,0}} B_{\alpha\alpha}(r_\beta)\,\mathrm{d}r_\beta, \tag{1}$$

where $\alpha = u$, v, or w, $\beta = x$, y, or z and $r_{\beta,0}$ is the first zero-crossing of the autocorrelation $B_{\alpha\alpha}(r_\beta) = \langle\alpha(x)\,\alpha(x+r_\beta)\rangle$ (Comte-Bellot and Corrsin, 1971). The majority of the parametric study measurements and all L_{uy} measurements were conducted at $x/M = 30$, with some other measurements investigating the effect of Re_M on constant grid conditions being conducted with SW3 and XW2 at $x/M = 41$. The significance of these measurements being conducted with different resolution and at a different location is discussed in section 4.

Measurements of the pressure drop across the grid were performed with a 10 Torr MKS pressure transducer con-

Table 1: Description of grid operational modes.

Mode	FR	CL	2FR	3FR	4CL	5FR	6CL	10CL
Front & aft mesh synchronized	No	Yes	No	No	Yes	No	Yes	Yes
Number of bars receiving same signal	0	2	2	3	4	5	6	10
Number of independent signals to grid	50	25	24	18	12	10	9	5

nected to static pressure ports upstream and downstream of the active grid. The pressure was sampled simultaneously with the velocity measurements, and thus was acquired over 4 minutes.

2.3 Estimation of turbulent quantities

The turbulent quantities used throughout this study are briefly defined here. Unless stated otherwise, the turbulence intensity was calculated based on $\left\langle q^2 \right\rangle$, where $\langle\cdot\rangle$ denotes a time-average. For convenience, we define the parameter T_q as

$$T_q = \frac{\left\langle q^2 \right\rangle^{1/2}}{3^{1/2} U}, \tag{2}$$

as the total turbulence intensity. The global isotropy was evaluated from the ratio $u'/v' = \left\langle u^2 \right\rangle^{1/2} / \left\langle v^2 \right\rangle^{1/2}$. The mean turbulent kinetic energy dissipation rate was estimated from

$$\langle \epsilon \rangle = 3\nu \left[\left\langle \left(\frac{\partial u}{\partial x} \right)^2 \right\rangle + 2 \left\langle \left(\frac{\partial v}{\partial x} \right)^2 \right\rangle \right], \tag{3}$$

which is based on the less restrictive assumption of local homogeneity rather than local isotropy. The Taylor microscale was similarly calculated allowing for variations from local isotropy with,

$$\lambda^2 = 5\nu \frac{\left\langle q^2 \right\rangle}{\langle \epsilon \rangle}, \tag{4}$$

and in turn the Taylor microscale Reynolds number was estimated from

$$Re_\lambda = \frac{\left\langle q^2 \right\rangle^{1/2} \lambda}{3^{1/2} \nu}. \tag{5}$$

The longitudinal integral scale, L_{ux}, was estimated using (1) and the autocorrelation based on the time-series of the u measurements. Finally, the normalised pressure drop across the grid is given by,

$$C_P = \frac{\Delta P}{\frac{1}{2}\rho U^2}, \tag{6}$$

where ΔP is the measured pressure drop.

2.4 Post-processing and uncertainty estimates

Post-processing was performed in order to improve the estimates of the statistical turbulent quantities. The successive filtering technique of Mi et al. (2005, 2011) was used to filter the data at the Kolmogorov frequency, $f_K = U/(2\pi\eta)$ in order to eliminate high-frequency noise. This technique involves estimating f_K, then applying a digital low-pass filter at f_K and updating the estimate of f_K until a converged value is reached. In the present analysis, a 9$^{\text{th}}$-order Butterworth filter was used to digitally filter at f_K. Convergence was typically reached in 4 or fewer iterations. Wyngaard-style corrections were made to the variances of the velocity fluctuations and velocity derivatives in order to minimize the error due to finite spatial resolution (Wyngaard, 1968; Zhu and Antonia, 1996; Hearst et al., 2012). Typical corrections for the velocity variances are ±0.5%, and corrections for the gradients may reach ±10% for the smallest η cases. A more detailed description of the post-processing used here is given by Hearst and Lavoie (2014).

Estimates of the measurement uncertainties are provided throughout this work as 'error bars' on the figures. In general, we only show a few error bars per figure to provide a visual representation of the uncertainty while keeping clutter low. If an error bar is not visible on an entire plot, then the uncertainty is contained within the symbol size. Uncertainties were estimated as the quadrature addition of the bias and random uncertainties. Random uncertainties were estimated using the boot-strapping technique described by Benedict and Gould (1996), and bias uncertainties were estimated from the break-down provided by Jørgensen (2002). Although the uncertainty changes marginally for each measurement, they are generally within the following bands: ±1% for U, ±2.5% for $\left\langle u^2 \right\rangle$, ±3% for $\left\langle v^2 \right\rangle$, ±5% for $\left\langle (\partial u/\partial x)^2 \right\rangle$, and ±6% for $\left\langle (\partial v/\partial x)^2 \right\rangle$. The uncertainty on more complex quantities was calculated based on standard error propagation rules and quadrature addition.

3 Influence of active grid parameters on the produced turbulence

The effect of the various adjustable parameters of the active grid are investigated here to determine their influence

on the produced turbulence. The present parametric study extends that conducted by Larssen and Devenport (2011), as the present apparatus has more adjustable parameters that can be varied over a greater range. In particular, we take many of the grid parameters to asymptotes not observed in previous studies, thus identifying where their influence becomes limited. As will be shown, it highlights the possibility of controlling certain features of the turbulence while allowing others to remain unchanged.

In this section, we first investigate the homogeneity of the flow field produced by the grid. We then briefly touch on parameters that do not have a significant influence on the flow, before individually addressing those that exert significant authority over the produced turbulence. Detailed results from this parametric study are tabulated in Appendix A. Any test referred to by name can be found there. Test names ending with an 'a' are conducted with square wings with holes, with a 'b' are conducted with solid square wings, and with a 'c' are conducted with solid circular wings.

3.1 Homogeneity

The homogeneity of the flow is assessed in Fig. 3. Two FR mode (V4a and V6a) and a 10CL mode (C13a) test case are considered. These cases were chosen because they are representative of the parameter space. In particular, C13a represents the 'worst-case' as it is the most correlated sequence, and V6a represents a high rotational rate fully random case. While the homogeneity of the streamwise turbulence intensity and the global isotropy fall within the uncertainty bounds for these two quantities for all three test cases, the mean velocity changes by nearly 3% within the investigation range for case C13a. The two FR mode cases have homogeneous U to within ±0.5%. The 10CL mode operation may effectively cause a shear region near the centreline of the tunnel because all the wings above the centreline receive the same signal, and all the wings below the centreline receive a different signal. The value of the correlation coefficient, $\langle uv \rangle / u'v'$ shown here is within the range measured in the far-field of regular grids, e.g., Isaza et al. (2014), for all three test cases. The two FR mode test cases shown have rotational rates of $\Omega \pm \omega = 3 \pm 2$ Hz (V4a) and $\Omega \pm \omega = 8 \pm 7$ Hz (V6a), thus identifying that the homogeneity is a consequence of the operational mode rather than Ω. The homogeneity of FR mode is verified over a larger range for V6a in Fig. 4, where the $z/M = 0$ homogeneity scan axis is plotted with the vertical scan from the transverse integral measurements, showing the homogeneity extends over at least the centre 50% of the tunnel height. While only the central region of the wind tunnel is assessed here, several other active grids have demonstrated that active grid turbulence is typically homogeneous when operated in a random mode unless measurements are performed in close proximity to the walls (Makita, 1991; Mydlarski and Warhaft, 1996; Poorte and Biesheuvel, 2002; Larssen and Devenport, 2011).

The only effect of correlating the motion of adjacent wings for this apparatus appears to be adversely changing the homogeneity. FR mode is thus used for all test cases, except those specifically investigating the influence of different correlated sequences, since FR mode produces the most homogeneous flow.

3.2 Parameters that do not affect the produced turbulence

The wing rotational period ($T \pm t$), i.e., the amount of time a wing moves in a given direction at a given rate before it receives a new signal, does not measurably influence the produced turbulence, as indicated by tests T1a-T6a in Table A2. As such, all other tests were conducted with $T \pm t \approx 2.1 \pm 2.0$ seconds, unless stated otherwise.

The rotational acceleration ($A \pm \alpha$) was also found to not significantly influence the produced turbulence. The particular tests designed to investigate the acceleration were A1a-A8a in Table A2. In these tests, the majority of the turbulence parameters were invariant with A within the uncertainty bounds of the experiment. Tests A1a and A3a do exhibit large values of L_{ux} relative to the other measurements, but a coherent trend is not discernible, suggesting those points are likely outliers. In further support of this hypothesis, the other streamwise length scale, L_{vx}, was constant to within ±5% and the uncertainty of our ability to estimate it for cases A1a-A8a. The present finding contrasts with the results of Larssen and Devenport (2011) who found that the turbulence intensity dropped by 0.6% (absolute) over the acceleration range 5 Hz/s to 20 Hz/s. In the present study, rotational accelerations in the range $0.5 \text{ Hz/s} \leq A \pm \alpha \leq 250 \text{ Hz/s}$ were investigated, significantly extending the investigation region for this parameter, and it was found that the previously observed trend may be absorbed into the scatter of the present measurements, revealing the produced turbulence was not affected in a systematic way by rotational acceleration.

The difference between FR and CL modes was rigorously assessed through test pairs V3a and S5a, V4a and S6a, and T1a and S7a. In general, it was found that there was no marked difference between operating the grid in FR mode or CL mode. The influence of the more correlated sequences was assessed through tests C1a-C13a. While Fig. 3 demonstrates that the correlated sequences produce a less homogeneous flow field (with respect to U only), these sequences have little to no effect on the other turbulence statistics. This result differs from that of Bewley et al. (2013) who were able to control the autocorrelation functions of the velocity components by correlating the motion of grid elements. We

attribute this discrepancy to their ability to control the rotation of pairs and tetrads of adjacent wings, thus creating a strong localized correlation in the initial generating conditions. Such correlation is not possible in the present grid because multiple wings are still mounted to a single rod.

The influence of the choice of random distribution function was investigated by tests G1a-G4a. For these tests, a Gaussian distribution was used rather than a top-hat. In general, it was found that the influence of the random distribution was not significant, and as such, all other tests were conducted with a top-hat distribution.

Finally, tests R1a-R3a assess the impact of forcing the rotation direction to change with each new command. When compared to test cases where this was not enforced, it was found that there was no systematic influence of applying this protocol.

3.3 Influence of the mean wing rotational rate

This section focusses on the influence of the wing rotational rate when the global Reynolds number is held constant at $Re_M \approx 39{,}000$. The instantaneous wing rotational rate was varied between 0.25 Hz and 20 Hz, and results are plotted in Fig. 5 versus the Rossby number ($Ro = U/\Omega M$). Fig. 5(a) shows that for $U/\Omega M > 50$ the turbulence reached a constant state whereby decreasing the rotational rate further did not change the turbulence intensity. However, for high values of Ω and Rossby numbers in the range $U/\Omega M < 50$, there was significant variability in the turbulence intensity. The $U/\Omega M = 50$ limit was not as well defined for Re_λ as demonstrated in Fig. 5(b). This is due to the dependence of Re_λ on λ, which also does not plateau as abruptly as the turbulence intensity (Fig. 5(e)). While the dissipative scales, given by η, remained approximately constant with Ω (Fig. 5(d)), the size of the large scales, L_{ux}, grew almost linearly with $U/\Omega M$ (Fig. 5(f)). The spanwise integral length scale, L_{uy} also grew linearly with $U/\Omega M$ as shown in Fig. 6, however, it was much smaller than L_{ux}, typically within $M \pm 15\%$.

A beneficial property of the turbulence produced by the grid was that the turbulence intensity was fairly constant while the size of the large scales (L_{ux}) continued to grow by a factor of 3.5 for the range $50 < U/\Omega M < 175$. This suggests that for a given turbulence intensity, one can change the mean rotational rate of the wings to tailor the size of the large scales in the flow; although, we note this necessitates a change in the global isotropy (Fig. 5(c)). Previous parametric studies have not exceeded $U/\Omega M \approx 50$, and as such this is the first time this asymptotic range has been reported.

In the region where turbulence intensity and the integral scale were independent, the global isotropy, u'/v', monotonically grew from ~ 1.3 to ~ 1.7 with increasing Ro. In order to assess what scales are affected by this increase in anisotropy, the measured second-order structure function of the spanwise velocity fluctuations, $\langle(\delta v)^2\rangle \equiv \langle(v(x+r)-v(x))^2\rangle$, can be compared to that calculated from the structure function from the streamwise velocity fluctuations, $\langle(\delta u)^2\rangle$, assuming isotropy, viz,

$$\langle(\delta v)^2\rangle_{\text{cal}} = \frac{r}{2}\frac{\mathrm{d}}{\mathrm{d}r}\langle(\delta u)^2\rangle + \langle(\delta u)^2\rangle. \tag{7}$$

This comparison is shown in Fig. 7 for one very anisotropic case V2b, where $u'/v' = 1.41$, and three other cases (V4b, V6b, and V11b) with similar anisotropy levels near $u'/v' = 1.23$. Despite the differing levels of anisotropy, all four tests have an approximately constant value of $\langle(\delta v)^2\rangle_{\text{cal}}/\langle(\delta v)^2\rangle \approx 1.3$ for $r/\lambda \lesssim 10$. The growth of the ratio at larger scales indicates that the bulk of the anisotropy was restricted to the largest scales of the flow. While the high levels of anisotropy for some cases limit the applicability of these modes for the study of 'homogeneous, isotropic turbulence', they are nonetheless useful for tailoring turbulence for other applications where homogeneity and isotropy are not the goal.

3.4 Influence of mean flow velocity

Table A1 provides results for tests conducted with both solid square and solid circular wings for different U. For each test case, the grid was set into motion with a particular setting, and the tunnel velocity was increased holding the probes stationary at $x/M = 41$. Fig. 8 shows different turbulence statistics versus the grid Reynolds number, Re_M. A caveat to consider when interpreting the results shown in Fig. 8 is that the non-dimensional parameters affecting the turbulent quantities are the Reynolds number Re_M and Rossby number Ro, as was previously found by Larssen and Devenport (2011). Clearly, both of these parameters vary when only U is changed. In order to help interpret the results of Fig. 8, contour plots of the turbulent quantities as a function of both Re and Ro^{-1} are given in Fig. 9 for the solid square wings case. The plot for the other wing geometries have the same trends and are thus not included.

The turbulence intensity appears to change with Re_M in Fig. 8(a). This dependence of T_q on Re_M is atypical compared to passive grid results. Generally for passive grids, the turbulent fluctuations scale with U, resulting in the independence of T_q with Re_M. This is evidenced by cases E1-E7 which are plotted as triangles in Fig. 8(a). The E1-E7 cases represent the turbulence produced by the grid when it was left in the fully open, non-actuated, position. T_q does not vary by more than 0.2% (absolute) over the same range of Re_M that sees variations of 2.2% (absolute) for the active cases. Fig. 10(a) demonstrates that C_P grew with Re_M for active grid cases U8b-U14b, which are representative of all cases, while it remained approximately constant for the open grid case. The relationship between C_P and T_q is shown to

be linear in Fig. 10(b) for the active case while for the open case the measurements were clustered at a single point on the C_P–T_q curve. However, this perceived dependence of T_q on Re_M is in fact a Ro effect (because U is in both parameters), as is evidenced by the iso-contours in Fig. 9(a) that are nearly horizontal (invariant with Re_M) but change drastically with Ro.

Both Fig. 8(b) and 9(b) show that Re_λ grew with Re_M as expected, however, the global isotropy in Fig. 8(c) reveals some interesting behaviour. The ratio u'/v' became approximately constant near 1.1 for $Re_M \geq 35{,}000$, except for the cases with the lowest Ω (U1-U7). This indicates that for a sufficient Re_M, the global isotropy becomes independent of Re_M for sufficiently high wing rotation rate.

As the mean velocity was increased, the size of the dissipative scales decreased as shown in Fig. 8(d), while Fig. 9(d) confirms the weak dependence on Ro seen in Fig. 5(d) over the full range of Re_M investigated here. Conversely, as the mean velocity was increased, the size of the longitudinal energy containing scales increased (Fig. 8(f)). This length scale only has a significant dependence on Ro for lower values of Ω as can be seen from Fig. 5(f) and 9(f). This behaviour represents an expansion of the physical size of the scales carrying the turbulence as Re_M increases, i.e., the large scales become larger and the small scales become smaller.

Fig. 11 plots different pre-multiplied spectra, kF_{11}, for constant grid settings but varying Re_M. The semi-logarithmic scale keeps the area under the curve equal to $\langle u^2 \rangle$, which provides a true representation of the distribution of the energy over the relevant scales (e.g., Lavoie et al., 2007). For each set of constant rotational parameters in Fig. 11(a) and 11(b) the peak of the pre-multiplied spectrum is approximately invariant with Re_M, both in magnitude and location. This implies that the energized wavenumbers were independent of Re_M. However, this independence was no longer satisfied at the lower values of Ω, as illustrated in Fig. 11(c) for cases U1b, U4b and U7b. These rotational settings are in the plateau region in Fig. 5(a), where T_q was constant, while u'/v' and L_{ux} grew, which is consistent with the trends visible in the spectra. This demonstrates that the fundamental structure of the turbulence changes when this plateau region is reached, as the flow behaves differently than at higher Ω.

3.5 Influence of wing geometry

Thormann and Meneveau (2014) identified that the wing geometry played a role in the produced turbulence in their study of the decay of active grid-generated turbulence with various fractal wings. However, they were unable to identify systematic trends linked to geometry. The present study allows us to comment further on the influence of wing geometry, at least at a fixed point.

For the same Rossby number, different wing shapes produced different turbulence intensities (Fig. 5(a)). The solid square wings always produced the highest intensities. The results of the solid circles and the squares with holes were very similar, but the solid circles consistently produced slightly higher levels of T_q.

The maximum blockage achievable by the solid square wings is 100%, however, the probability of this happening was extremely low. The equivalent maximum possible blockage for the squares with holes and the solid circles is 79% and 78%, respectively. The proximity of the frontal area of the squares with holes and the circles to each other and the small differences in their results suggests that the influence of the wing geometry was likely caused by blockage rather than the shape itself.

From the other plots in Fig. 5, except Re_λ, which follows the same trend as T_q, it is evident that the remaining parameters appear to be relatively independent of the wing geometry. Isotropy and the size of the scales in the flow scaled with Rossby number and not with the wing geometry. This was also true of the transverse integral length scale shown in Fig. 6. These results are confirmed by Fig. 8. Hence, the effect of the wings was to change the T_q and Re_λ and this effect is linked to their respective blockage ratio.

4 Influence of initial conditions on spectral shape

The active grid presents a unique opportunity for grid turbulence measurements in that the same Re_λ can be produced using different sets of initial conditions over a broad range of Re_λ, that exceed those achievable by passive grids, and without necessitating large changes in Re_M. In Fig. 12, 15 tests at 5 different Re_λ, spanning $177 \leq Re_\lambda \leq 486$, are compared. The selected test cases employ a variety of different initial conditions, including: use of two operational modes (FR and CL), a wide range of mean rotational rates (0.625 Hz $\leq \Omega \leq$ 17.5 Hz), all three wing geometries, and a range of grid Reynolds numbers ($36{,}000 \leq Re_M \leq 55{,}000$). The measurements were conducted at two different streamwise positions ($x/M = 30$ and 41), and with both 0.6 and 1.1 mm sensing length hot-wires. Hence, the test cases shown in Fig. 12 represent a broad range of the initial generating conditions and measurement conditions.

The inner variable normalized spectra of Fig. 12 illustrate that the turbulence spectra generated by different initial conditions were collapsed for a given Re_λ in the range $k\eta > 10^{-3}$. The variation of the scaling exponent, k^m, in the scaling range is always less than ±1.2% for a given Re_λ. The scaling exponent did display a dependence on Re_λ as it changed from $m = -1.42$ to -1.56 over the investigated range. The lower limit of which is near, but not exactly, Kolmogrov's $k^{-5/3}$ prediction. This is in general agreement with the trends found by Mydlarski and Warhaft (1996). The

scaling exponent, m, was measured over $0.004 \leq k\eta \leq 0.05$, which was found to be within the scaling range for all active grid test cases. From the illustrated spectra in Fig. 12 and the minimal variations in m, it is clear that the spectra were well collapsed in the scaling and dissipative ranges at a given Re_λ for the active grid.

The spectra at constant Re_λ only differ from one-another at low wavenumbers, which are associated with the large scales. For instance, at $Re_\lambda \approx 485$, case U7b ($\Omega \pm \omega = 0.625 \pm 0.375$ Hz) has a broadband peak at low wavenumbers that differs from U14b ($\Omega \pm \omega = 3 \pm 2$ Hz). This difference is associated with the dependence of the energy peak on Ω, as indicated in Fig. 11. By comparison of the results presented in Table A1, these two test cases have approximately the same η and λ, but L_{ux} for U7b was nearly twice that of U14b. The integral scale is a large scale parameter. Furthermore, the global isotropy, which is also a large scale parameter, for U7b was $u'/v' = 1.46$, while it was 1.12 for U14b. These comparisons quantitively illustrate that the spectra and flow differ only at the large scales, while their small scales remain approximately the same for a given Re_λ.

These results suggest that for these Re_λ and reasonably homogeneous and isotropic turbulence, the structure of the turbulence itself has predominately 'forgotten' its initial conditions, and any remnants of them are carried only in the largest scales.

5 Conclusions

A new active grid with a greater number of elements across the tunnel cross-section and that has decoupled the motion of adjacent wings was used to extend earlier parametric studies to include higher Rossby numbers, $Ro = U/\Omega M$, and different wing geometries. The three parameters shown to have the greatest influence on the produced turbulence were Ro, Re_M, and wing blockage. It was shown that for $Ro > 50$, an asymptotic state was reached in turbulence intensity and Re_λ whereby increasing Ro further had no impact on these properties. However, if Ro was increased by decreasing Ω and holding U constant, then anisotropy and L_{ux} both grew. Hence, in this asymptotic state, a certain degree of control authority could be exerted over the size of the largest scales for a given turbulence intensity, provided a loss in isotropy was acceptable. For moderate and high Ω, the global isotropy reached an asymptote near $u'/v' = 1.1$ for $Re_M > 35{,}000$. The effect of the anisotropy, felt mostly for low values of Ω, was shown to be contained primarily in scales larger than 10λ. Consistent with this observation, both the Kolmogorov and Taylor microscales were only weakly dependent on Ro and primarily changed with Re_M. Solid square wings consistently produced the highest turbulence intensities and Re_λ, while circular wings and square wings with holes produced lower values. This was linked to the effective maximum blockage of the various wing geometries. It was further identified that the isotropy, and size of the scales was relatively independent of wing geometry.

It was also observed that the high wavenumber spectra were nearly identical for approximately homogeneous turbulence at a given Re_λ. This was verified for turbulence at the same Re_λ, over the range $177 \leq Re_\lambda \leq 486$, produced with considerably different active grid conditions. This suggests that the small scale turbulence organization is approximately independent of its initial conditions for a given Re_λ in homogeneous and approximately isotropic turbulence, in agreement with theoretical expectations. Furthermore, it was identified that any differences that do remain in the produced turbulence spectrum are isolated to the largest scales, and carried in ensemble parameters such u'/v' and L_{ux}.

Acknowledgements This project was funded through a Natural Sciences and Engineering Research Council of Canada (NSERC) Engage grant in collaboration with Anemoi Technologies Inc., specialists in simulation and test facilities. RJH acknowledges financial support from the Ontario Provincial Government and NSERC. The authors would like to thank Mr. S. Ciurzynski of Anemoi Technologies Inc. who aided in the design and manufacturing of the active grid. Special appreciation is given to Mr. R. Santos Baptista who aided with the data acquisition, and to Ms. E. Dogan and Prof. B. Ganapathisubramani for insightful comments on the spectra.

References

L. H. Benedict and R. D. Gould. Towards better uncertainty estimates for turbulence statistics. *Exp. Fluids*, 22:129–136, 1996.

G. P. Bewley, J. Kassel, and E. Bodenschatz. Control of turbulence with a high degree-of-freedom active grid. In *14th European Turbulence Conference*, 2013.

E. Bodenschatz, G. P. Bewley, H. Nobach, M. Sinhuber, and H. Xu. Variable density turbulence tunnel facility. *Rev. Sci. Inst.*, 85(093908), 2014.

P. Burattini and R. A. Antonia. The effect of different X-wire calibration schemes on some turbulence statistics. *Exp. Fluids*, 38:80–89, 2005.

R. B. Cal, J. Lebrón, L. Castillo, H. S. Kang, and C. Meneveau. Experimental study of the horizontally averaged flow structure in a model wind-turbine array boundary layer. *J. Renewable Sustain. Energy*, 2(013106), 2010.

H. E. Cekli and W. van de Water. Tailoring turbulence with an active grid. *Exp. Fluids*, 49:409–416, 2010.

G. Comte-Bellot and S. Corrsin. The use of a contraction to improve the isotropy of grid-generated turbulence. *J. Fluid Mech.*, 25(4):657–682, 1966.

G. Comte-Bellot and S. Corrsin. Simple Eulerian time correlation of full- and narrow-band velocity signals in grid-generated, 'isotropic' turbulence. *J. Fluid Mech.*, 48:273–337, 1971.

R. J. Hearst and P. Lavoie. Decay of turbulence generated by a square-fractal-element grid. *J. Fluid Mech.*, 741:567–584, 2014.

R. J. Hearst, O. R. H. Buxton, B. Ganapathisubramani, and P. Lavoie. Experimental estimation of fluctuating velocity and scalar gradients in turbulence. *Exp. Fluids*, 53(4): 925–942, 2012.

J. C. Isaza, R. Salazar, and Z. Warhaft. On grid-generated turbulence in the near- and far field regions. *J. Fluid Mech.*, 753:402–426, 2014.

F. E. Jørgensen. *How to measure turbulence with hot-wire anemometers - a practical guide*. Dantec Dynamics, 2002.

H.S. Kang, S. Chester, and C. Meneveau. Decaying turbulence in an active-grid-generated flow and comparisons with large-eddy simulation. *J. Fluid Mech.*, 480:129–160, 2003.

P. Knebel, A. Kittel, and J. Peinke. Atmospheric wind field conditions generated by active grids. *Exp. Fluids*, 51: 471–481, 2011.

A. N. Kolmogorov. The local structure of turbulence in incompressible viscous fluids for very large Reynolds numbers. *Dokl. Akad. Nauk SSSR*, 30(4):301–305, 1941.

J. V. Larssen and W. J. Devenport. On the generation of large-scale homogeneous turbulence. *Exp. Fluids*, 50: 1207–1223, 2011.

P. Lavoie, L. Djenidi, and R. A. Antonia. Effects of initial conditions in decaying turbulence generated by passive grids. *J. Fluid Mech.*, 585:395–420, 2007.

H. Makita. Realization of a large-scale turbulence field in a small wind tunnel. *Fluid Dyn. Res.*, 8:53–64, 1991.

J. Mi, R. C. Deo, and G. J. Nathan. Fast-convergence iterative scheme for filtering velocity signals and finding Kolmogorov scales. *Phys. Rev. E*, 71(066304), 2005.

J. Mi, M. Xu, and C. Du. Digital filter for hot-wire measurements of small-scale turbulence properties. *Meas. Sci. Tech.*, 22(125401), 2011.

I. S. Miller, D. A. Shah, and R. A. Antonia. A constant temperature hot-wire anemometer. *J. Phys. E: Sci. Instrum.*, 20:311–314, 1987.

L. Mydlarski and Z. Warhaft. On the onset of high-Reynolds-number grid-generated wind tunnel turbulence. *J. Fluid Mech.*, 320:331–368, 1996.

L. Mydlarski and Z. Warhaft. Passive scalar statistics in high-Péclet-number grid turbulence. *J. Fluid Mech.*, 358: 135075, 1998.

R.E.G. Poorte and A. Biesheuvel. Experiments on the motion of gas bubbles in turbulence generated by an active grid. *J. Fluid Mech.*, 461:127–154, 2002.

N. Sharp, S. Neuscamman, and Z. Warhaft. Effects of large-scale free stream turbulence on a turbulent boundary layer. *Phys. Fluids*, 21(095105), 2009.

M. J. Sytsma and L. Ukeiley. Mean loads from wind-tunnel turbulence on low-aspect-ratio flat plates. *J. Aircraft*, 50 (3):863–870, 2013.

A. Thormann and C. Meneveau. Decay of homogeneous, nearly isotropic turbulence behind active fractal grids. *Phys. Fluids*, 26(025112), 2014.

J. C. Wyngaard. Measurements of small-scale turbulence structure with hot wires. *J. Sci. Instr.*, 1(2):1105–1108, 1968.

Y. Zhu and R. A. Antonia. The spatial resolution of hot-wire arrays for the measurement of small-scale turbulence. *Meas. Sci. Tech.*, 7:1349–1359, 1996.

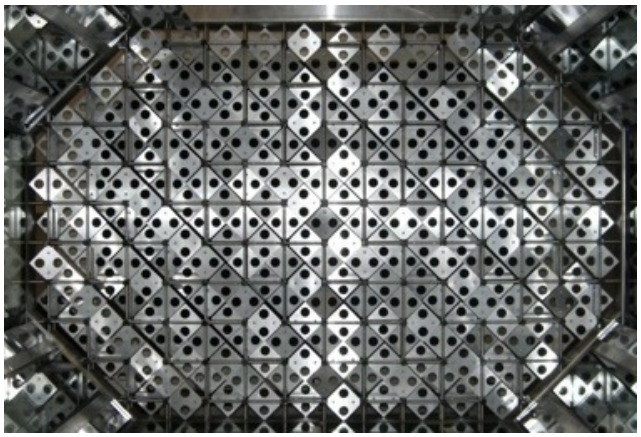

(a)

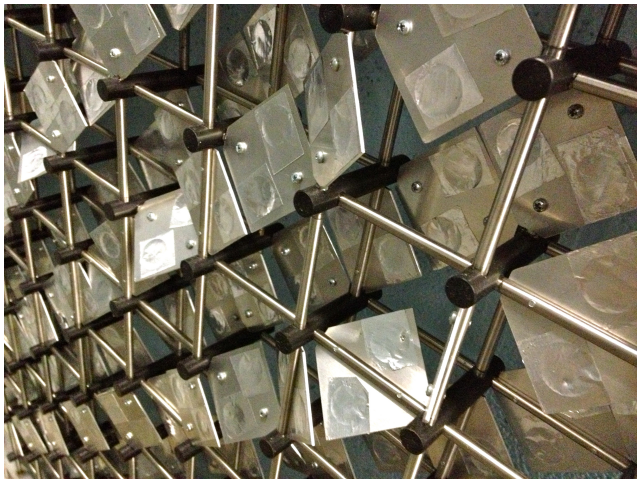

(b)

Fig. 1: Photographs of the active grid (a) *in situ* and (b) showing the double-mesh design.

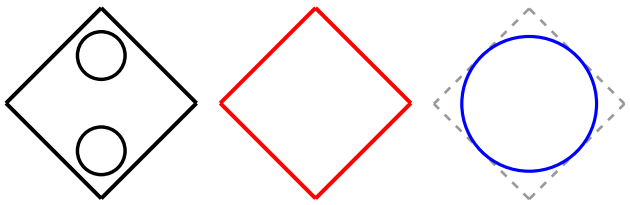

(a) (b) (c)

Fig. 2: Schematics of the active grid wing geometries: (a) 55 mm × 55 mm squares with dia. 20 mm holes, (b) 55 mm × 55 mm solid squares, and (c) dia. 55 mm circles.

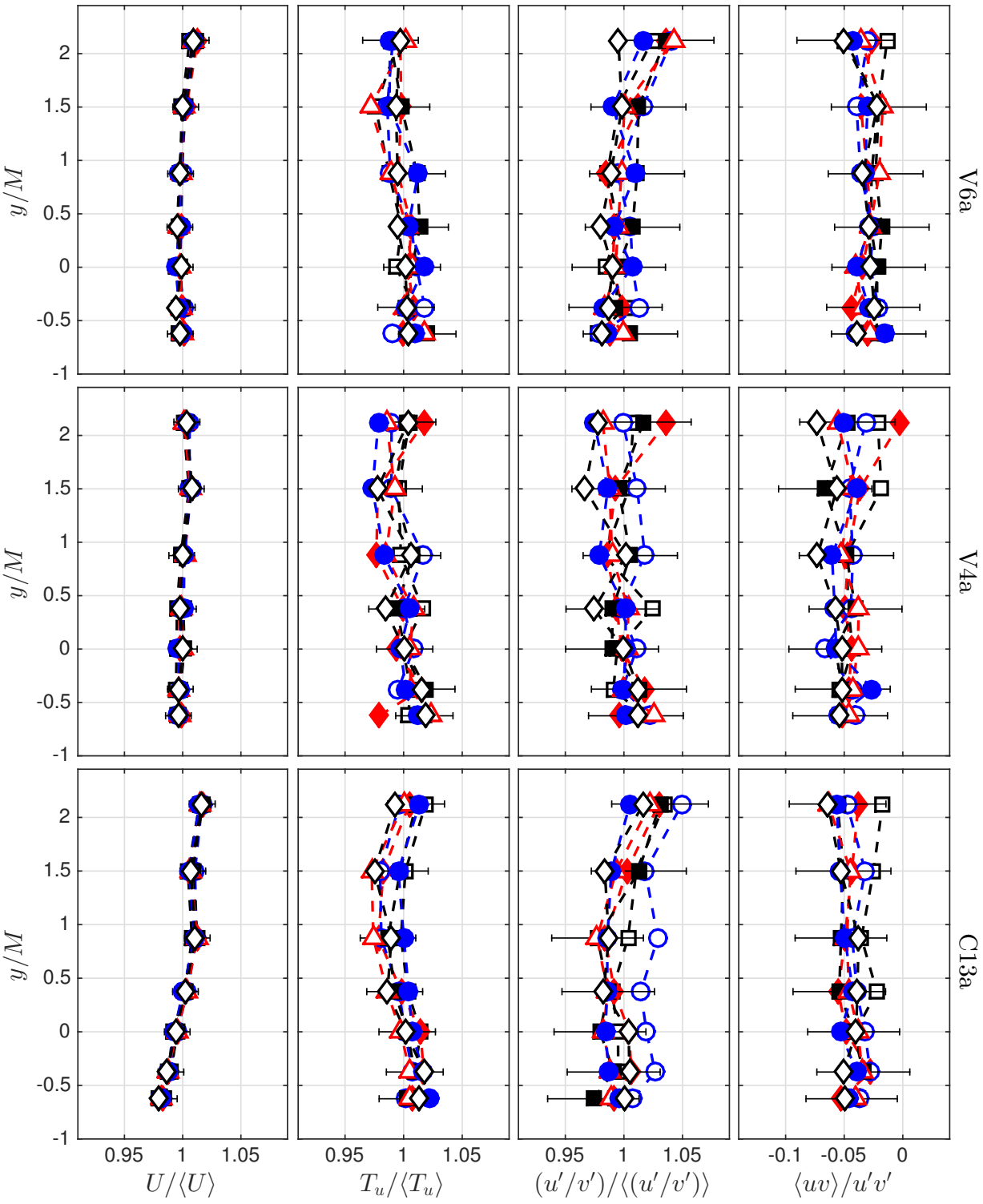

Fig. 3: Homogeneity profiles of the (from left to right) mean velocity, streamwise turbulence intensity, global isotropy, and normalised Reynolds shear stress, for test cases (from top to bottom) V6a, V4a, and C13a. All scans were performed at $x/M = 30$. (□) $z/M = -11/8$, (♦) $z/M = -7/8$, (○) $z/M = -3/8$, (■) $z/M = 0$, (△) $z/M = 3/8$, (●) $z/M = 7/8$, (◇) $z/M = 11/8$.

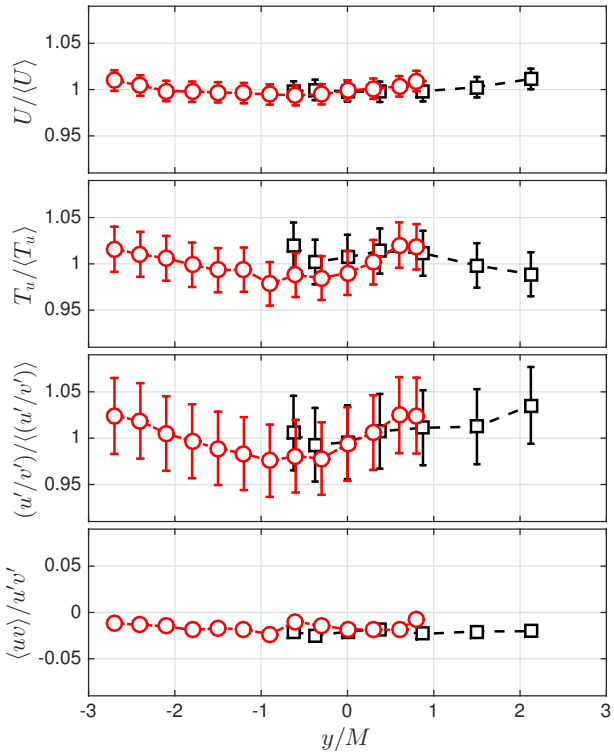

Fig. 4: Homogeneity scan over an extended range for test case V6a. (○) from transverse integral scale measurements, (□) from $z/M = 0$ axis of planar homogeneity scans.

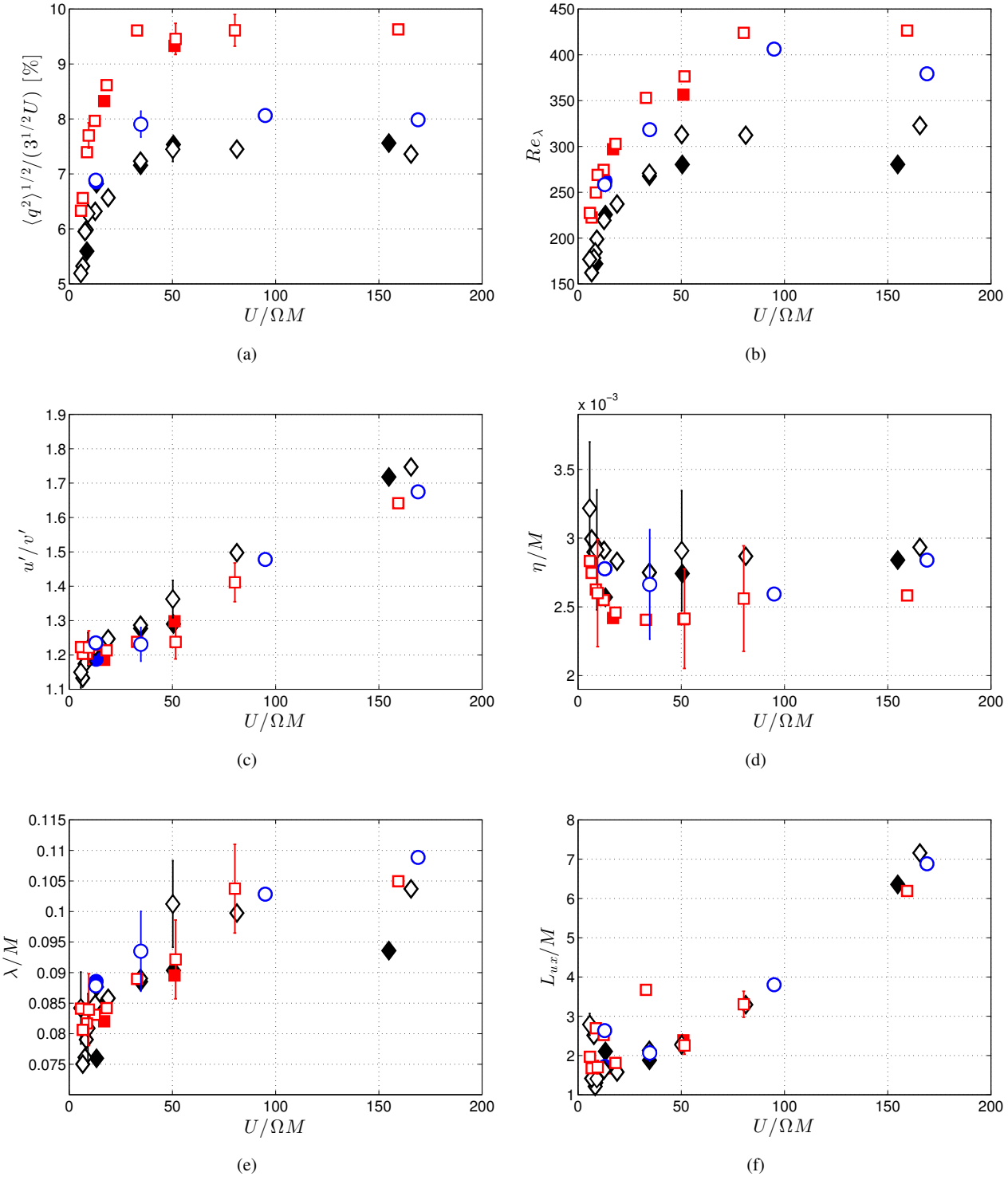

Fig. 5: Variation of turbulence properties with Rossby number, $Ro = U/\Omega M$. In all cases here, Ω was the only quantity varied in Ro, i.e., both U and M were held constant. (◇) square wings with holes, (□) solid square wings, (○) solid circular wings; empty symbols are tests in FR mode, and filled symbols are tests in CL mode. Test cases included here are V1-V11a,b,c and T1a,b. Error bars illustrate the typical uncertainty associated with the measurement of these parameters.

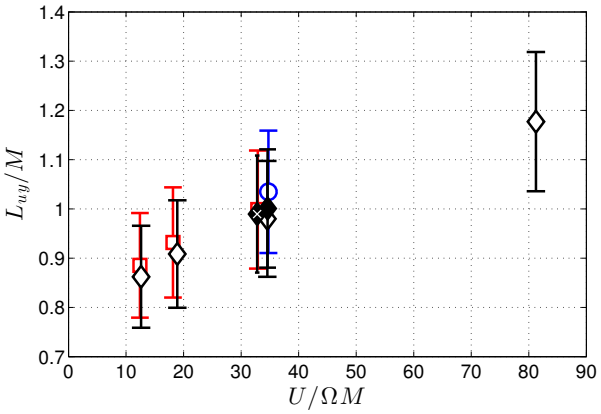

Fig. 6: Spanwise integral length scale, L_{uy}, for changing Rossby number, $Ro = U/\Omega M$. In all cases here, Ω was the only quantity varied in Ro, i.e., both U and M were held constant. (◇) square wings with holes, (□) solid square wings, (○) solid circular wings; empty symbols are tests in FR mode, filled symbols are tests in CL mode, and filled symbols with a '×' are tests in 10CL mode.

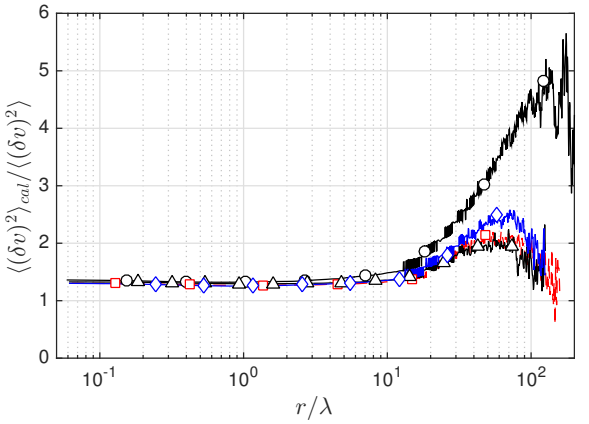

Fig. 7: Ratio of the estimated isotropic transverse second-order structure function to the measured transverse second-order structure function. (○) V2b, $u'/v' = 1.41$; (◇) V4b, $u'/v' = 1.24$; (□) V6b, $u'/v' = 1.23$; (△) V11b, $u'/v' = 1.22$.

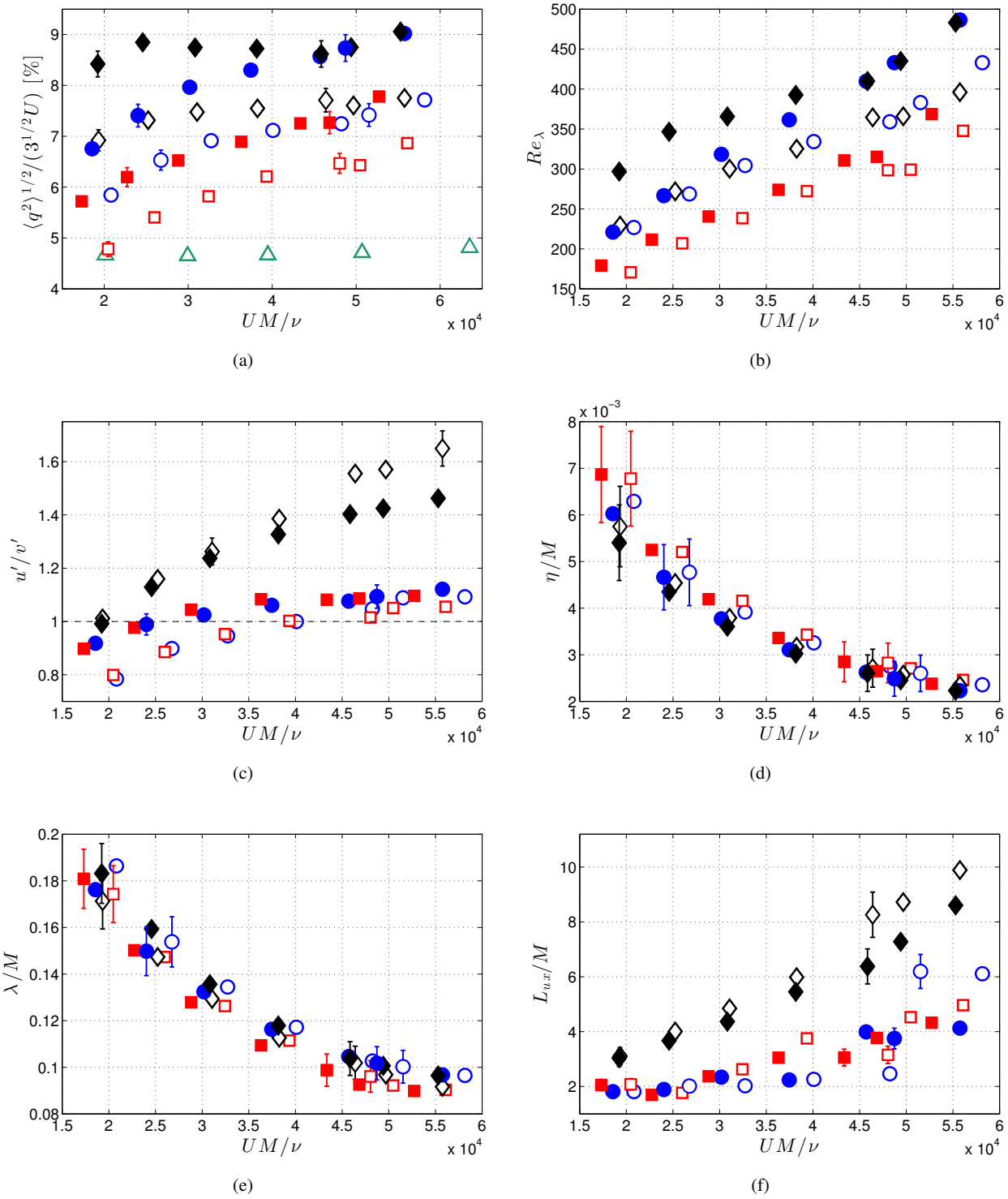

Fig. 8: Relationship between turbulence properties and the grid Reynolds number, $Re_M = UM/\nu$. For each case shown, U was the only quantity varied. (◇) U1-U7, (○) U8-U14, (□) U15-U21, (△) open grid cases E1-E7 offset by +3%; filled symbols represents solid square wings ('b' cases), and empty symbols represent solid circular wings ('c' cases).

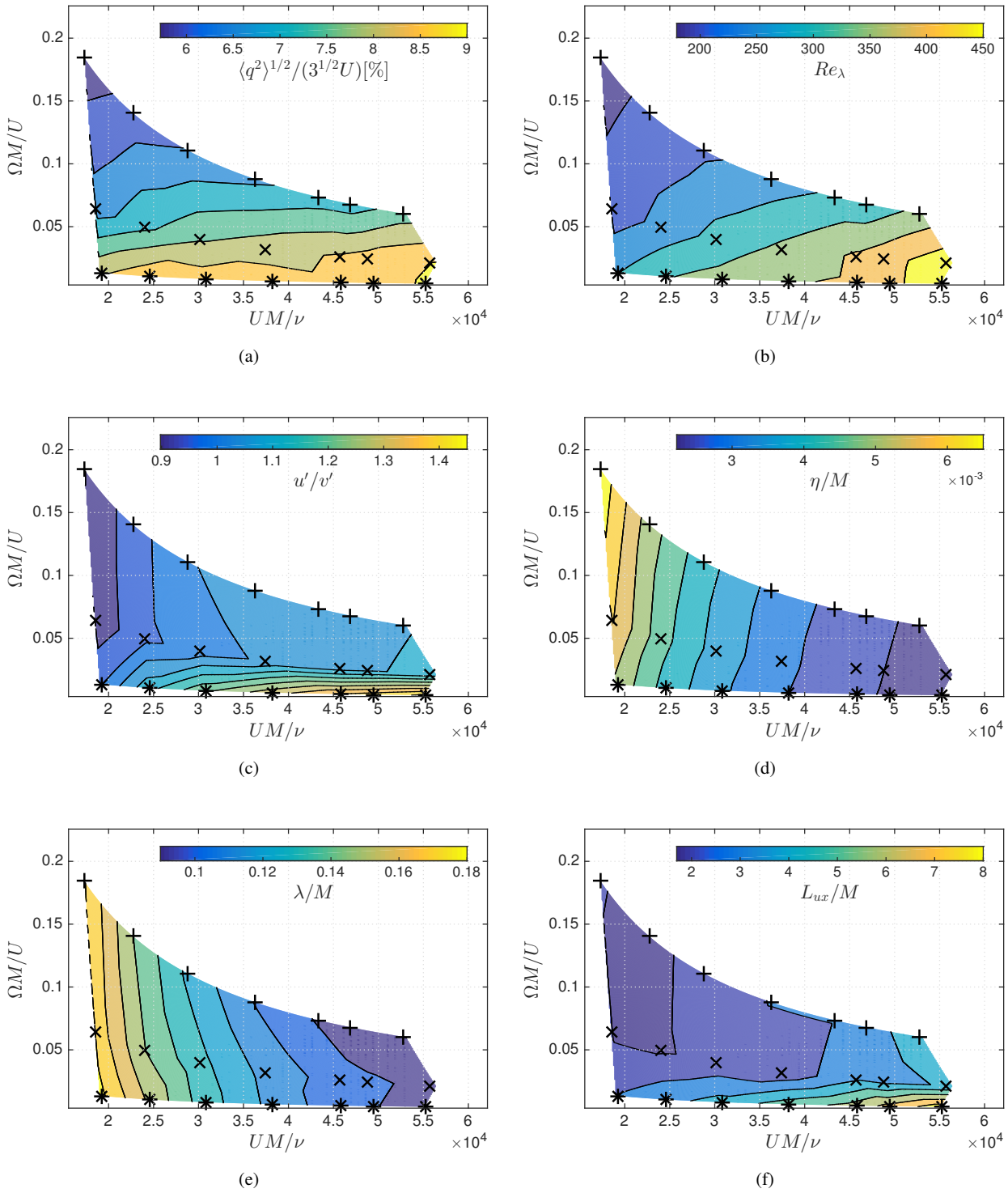

Fig. 9: Contours identifying the co-dependence of the produced turbulence on the Reynolds number and the Rossby number (plotted in inverse). Contours are drawn for solid square wings. (∗) U1b to U7b, $\Omega \pm \omega = 0.625 \pm 0.375$ Hz; (×) U8b to U14b, $\Omega \pm \omega = 3 \pm 2$ Hz; (+) U15b to U21b, $\Omega \pm \omega = 8 \pm 7$ Hz.

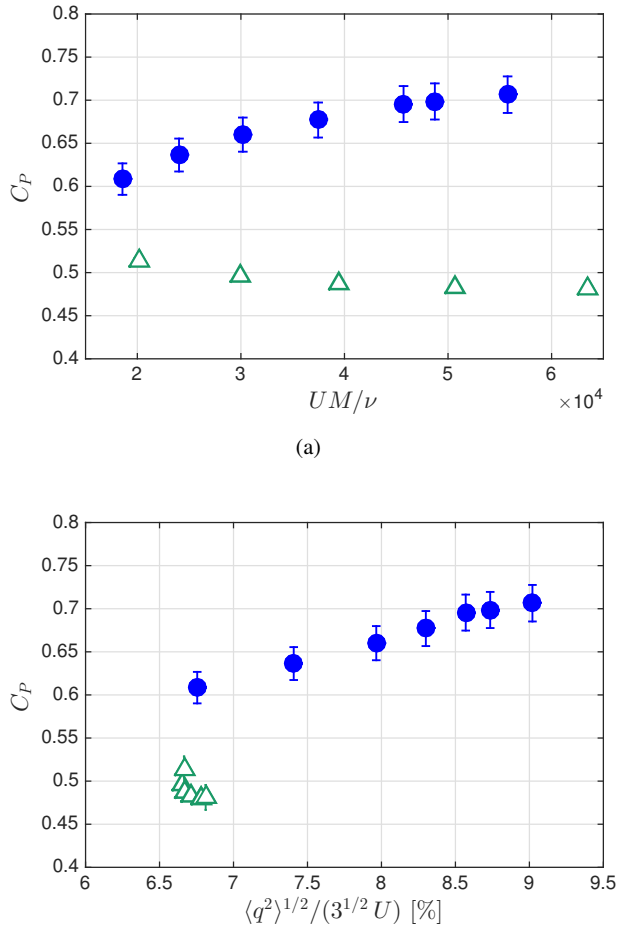

Fig. 10: Non-dimensional pressure drop across the grid compared to (a) grid Reynolds number, and (b) turbulence intensity. For each case shown, U was the only quantity varied. (●) U8b-U14b, (△) open grid cases E1-E7 with C_p offset by +0.4 and T_q offset by +5%.

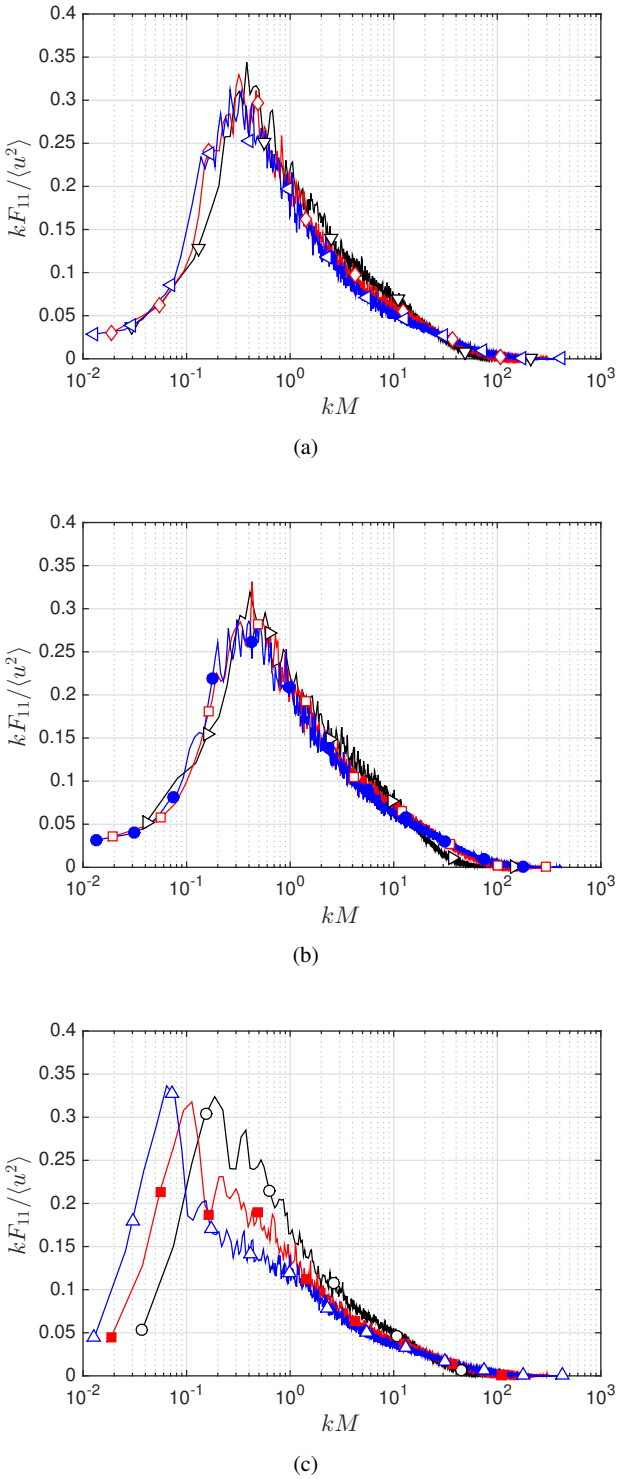

Fig. 11: Pre-multiplied spectra comparing cases with the same grid parameters but different Re_M. (a) Cases with $\Omega \pm \omega = 3 \pm 2$ Hz: (▽) U9b, $Re_M = 24{,}000$; (◇) U11b, $Re_M = 37{,}500$; (◁) U14b, $Re_M = 55{,}800$. (b) Cases with $\Omega \pm \omega = 8 \pm 7$ Hz: (▷) U15b, $Re_M = 17{,}300$; (□) U18b, $Re_M = 36{,}300$; (●) U21b, $Re_M = 52{,}700$. (c) Cases with $\Omega \pm \omega = 0.625 \pm 0.375$ Hz: (○) U1b, $Re_M = 19{,}200$; (■) U4b, $Re_M = 38{,}200$; (△) U7b, $Re_M = 55{,}300$

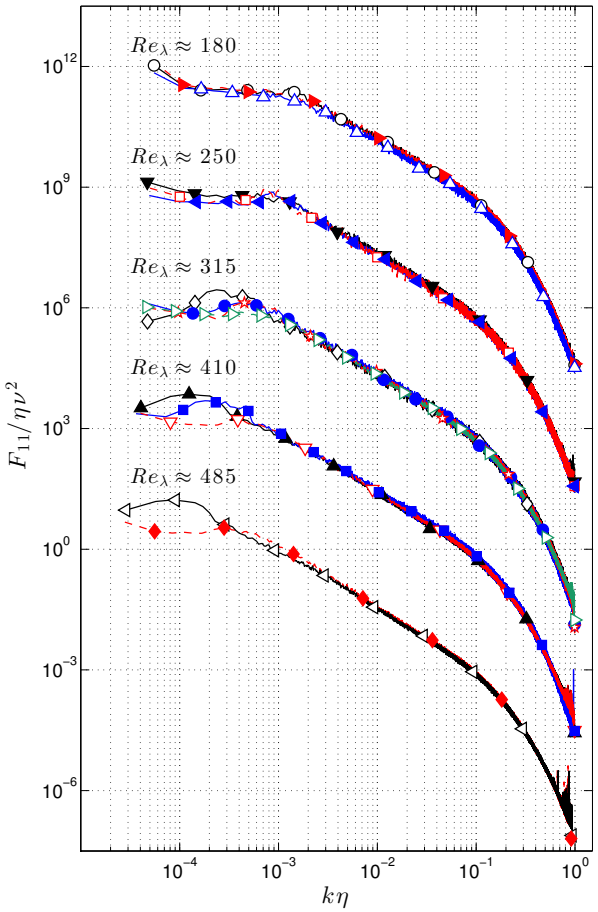

Fig. 12: Inner variable normalized spectra at the same Re_λ but produced by different initial conditions. Each set of curves is offset by 10^{-3}, starting from the $Re_\lambda \approx 180$ case. (○) V8a, $Re_\lambda = 185$; (▶) V9a, $Re_\lambda = 178$; (△) V11a, $Re_\lambda = 177$; (▼) V8b, $Re_\lambda = 250$; (□) C13a, $Re_\lambda = 250$; (◀) A7a, $Re_\lambda = 249$; (◇) V2a, $Re_\lambda = 312$; (★) V3a, $Re_\lambda = 312$; (●) V4c, $Re_\lambda = 318$; (▷) U19b, $Re_\lambda = 311$; (▲) U5b, $Re_\lambda = 410$; (▽) U12b, $Re_\lambda = 410$; (■) V2c, $Re_\lambda = 406$; (◁) U7b, $Re_\lambda = 483$; (♦) U14b, $Re_\lambda = 486$.

Appendix A: Supplemental parametric study tables

Table A1: The effect of mean velocity on the produced turbulence. Measurements performed at $x/M = 41$.

Case	Mode	Ro	Re_M $\times 10^3$	$\Omega \pm \omega$ [Hz]	U [m/s]	T_q [%]	Re_λ	u'/v'	η/M	λ/M	L_{ux}/M	C_P
U1b	FR	76	18.4	0.625 ± 0.375	3.8	8.4	297	0.99	0.0054	0.183	3.04	0.64
U2b	FR	98	23.7	0.625 ± 0.375	4.9	8.8	346	1.13	0.0043	0.159	3.67	0.67
U3b	FR	122	29.5	0.625 ± 0.375	6.1	8.7	366	1.24	0.0036	0.136	4.36	0.70
U4b	FR	152	36.8	0.625 ± 0.375	7.6	8.7	393	1.33	0.0030	0.118	5.45	0.72
U5b	FR	182	44.1	0.625 ± 0.375	9.1	8.6	410	1.40	0.0026	0.104	6.38	0.74
U6b	FR	198	47.9	0.625 ± 0.375	9.9	8.8	435	1.42	0.0025	0.101	7.28	0.74
U7b	FR	222	53.8	0.625 ± 0.375	11.1	9.1	483	1.46	0.0022	0.096	8.60	0.76
U8b	FR	15	17.9	3.0 ± 2.0	3.7	6.8	221	0.92	0.0060	0.176	1.81	0.61
U9b	FR	20	23.2	3.0 ± 2.0	4.8	7.4	267	0.99	0.0047	0.150	1.89	0.64
U10b	FR	25	29.5	3.0 ± 2.0	6.1	8.0	318	1.02	0.0038	0.132	2.34	0.66
U11b	FR	32	36.8	3.0 ± 2.0	7.6	8.3	362	1.06	0.0031	0.116	2.24	0.68
U12b	FR	38	44.6	3.0 ± 2.0	9.2	8.6	410	1.08	0.0026	0.105	3.99	0.70
U13b	FR	41	47.9	3.0 ± 2.0	9.9	8.7	433	1.09	0.0025	0.102	3.75	0.70
U14b	FR	47	54.7	3.0 ± 2.0	11.3	9.0	486	1.12	0.0022	0.097	4.13	0.71
U15b	FR	5	17.0	8.0 ± 7.0	3.5	5.7	179	0.90	0.0069	0.181	2.05	0.70
U16b	FR	7	22.3	8.0 ± 7.0	4.6	6.2	212	0.98	0.0052	0.150	1.69	0.70
U17b	FR	9	28.1	8.0 ± 7.0	5.8	6.5	241	1.04	0.0042	0.128	2.37	0.72
U18b	FR	11	35.4	8.0 ± 7.0	7.3	6.9	274	1.08	0.0034	0.109	3.05	0.73
U19b	FR	14	42.1	8.0 ± 7.0	8.7	7.3	311	1.08	0.0028	0.099	3.05	0.74
U20b	FR	15	45.5	8.0 ± 7.0	9.4	7.3	315	1.09	0.0026	0.093	3.77	0.74
U21b	FR	17	51.8	8.0 ± 7.0	10.7	7.8	369	1.10	0.0024	0.090	4.32	0.75
U1c	FR	78	18.9	0.625 ± 0.375	3.9	6.9	229	1.01	0.0058	0.171	3.10	0.55
U2c	FR	102	24.7	0.625 ± 0.375	5.1	7.3	272	1.16	0.0045	0.147	4.01	0.59
U3c	FR	126	30.5	0.625 ± 0.375	6.3	7.5	300	1.26	0.0038	0.129	4.85	0.61
U4c	FR	156	37.8	0.625 ± 0.375	7.8	7.6	325	1.39	0.0032	0.113	5.99	0.62
U5c	FR	190	46.0	0.625 ± 0.375	9.5	7.7	364	1.56	0.0027	0.102	8.26	0.63
U6c	FR	204	49.4	0.625 ± 0.375	10.2	7.6	366	1.57	0.0026	0.097	8.72	0.63
U7c	FR	228	55.2	0.625 ± 0.375	11.4	7.8	396	1.65	0.0023	0.092	9.89	0.64
U8c	FR	18	20.8	3.0 ± 2.0	4.3	5.8	227	0.78	0.0063	0.186	1.82	0.47
U9c	FR	23	26.6	3.0 ± 2.0	5.5	6.5	269	0.90	0.0048	0.154	2.01	0.50
U10c	FR	28	32.4	3.0 ± 2.0	6.7	6.9	304	0.95	0.0039	0.134	2.03	0.53
U11c	FR	35	40.2	3.0 ± 2.0	8.3	7.1	334	1.00	0.0033	0.117	2.26	0.54
U12c	FR	41	47.9	3.0 ± 2.0	9.9	7.2	359	1.05	0.0028	0.103	2.46	0.57
U13c	FR	44	51.3	3.0 ± 2.0	10.6	7.4	383	1.09	0.0026	0.100	6.20	0.57
U14c	FR	50	58.1	3.0 ± 2.0	12.0	7.7	433	1.09	0.0024	0.096	6.11	0.58
U15c	FR	7	20.3	8.0 ± 7.0	4.2	4.8	171	0.80	0.0068	0.174	2.08	0.50
U16c	FR	8	25.7	8.0 ± 7.0	5.3	5.4	207	0.89	0.0052	0.147	1.77	0.51
U17c	FR	10	32.4	8.0 ± 7.0	6.7	5.8	238	0.95	0.0042	0.126	2.63	0.53
U18c	FR	13	39.2	8.0 ± 7.0	8.1	6.2	272	1.00	0.0034	0.111	3.75	0.55
U19c	FR	15	47.9	8.0 ± 7.0	9.9	6.5	298	1.01	0.0028	0.096	3.15	0.56
U20c	FR	16	50.4	8.0 ± 7.0	10.4	6.4	299	1.05	0.0027	0.092	4.53	0.56
U21c	FR	18	56.2	8.0 ± 7.0	11.6	6.9	348	1.05	0.0025	0.090	4.97	0.57
E1	Open	–	19.9	–	4.1	1.7	45	0.89	0.0101	0.134	1.64	0.11
E2	Open	–	29.5	–	6.1	1.6	50	1.00	0.0073	0.102	2.34	0.10
E3	Open	–	38.7	–	8.0	1.7	57	1.00	0.0058	0.086	3.00	0.09
E4	Open	–	49.9	–	10.3	1.7	65	1.01	0.0047	0.075	5.77	0.08
E5	Open	–	63.0	–	13.0	1.8	80	1.03	0.0040	0.070	7.82	0.08
E6	Open	–	67.8	–	14.0	1.8	80	1.06	0.0037	0.066	7.11	0.08
E7	Open	–	78.0	–	16.1	1.8	85	1.05	0.0034	0.061	8.10	0.08

Table A2: Grid and flow properties for test cases with square wings with holes. All measurements were performed at $x/M = 30$.

Case	Mode	Ro	Re_M $\times 10^3$	$T \pm t$ [s]	$\Omega \pm \omega$ [Hz]	$A \pm \alpha$ [Hz/s]	U [m/s]	T_q [%]	Re_λ	$\langle\epsilon\rangle M/U^3$ $\times 10^3$	u'/v'	η/M	λ/M	L_{ux}/M	L_{vx}/M	L_{uy}/M
T1a	FR	17	38.7	2.11 ± 2.07	6.0 ± 4.0	125	8.0	6.8	241	0.23	1.15	0.0028	0.085	1.41	0.98	
T2a	FR	17	38.7	2.12 ± 2.07	6.0 ± 4.0	125	8.0	6.6	226	0.23	1.19	0.0028	0.082	1.41	0.75	
T3a	FR	17	38.7	2.48 ± 2.44	6.0 ± 4.0	125	8.0	6.6	227	0.23	1.15	0.0028	0.083	1.33	0.83	
T4a	FR	17	38.7	3.18 ± 3.14	6.0 ± 4.0	125	8.0	6.7	235	0.22	1.17	0.0028	0.084	1.42	0.83	
T5a	FR	17	39.2	5.40 ± 5.36	6.0 ± 4.0	125	8.1	6.6	236	0.22	1.14	0.0028	0.085	1.31	0.85	
T6a	FR	17	38.7	7.78 ± 2.69	6.0 ± 4.0	125	8.0	6.7	237	0.22	1.13	0.0028	0.086	1.28	0.86	
V1a	FR	166	40.2	2.11 ± 2.02	0.625 ± 0.375	125	8.3	7.4	323	0.18	1.75	0.0028	0.092	7.16	2.07	
V2a	FR	81	39.2	2.11 ± 2.06	1.25 ± 0.75	125	8.1	7.5	312	0.20	1.50	0.0027	0.089	3.29	1.61	1.18
V3a	FR	50	38.7	2.11 ± 2.06	2.0 ± 1.0	125	8.0	7.4	312	0.20	1.36	0.0027	0.090	2.27	1.27	
V4a	FR	35	40.2	2.12 ± 2.04	3.0 ± 2.0	250	8.3	7.2	271	0.24	1.29	0.0028	0.089	2.13	1.08	0.98
V5a	FR	19	40.2	2.17 ± 2.01	5.5 ± 4.5	250	8.3	6.6	237	0.21	1.25	0.0028	0.086	1.58	0.80	0.91
V6a	FR	13	39.2	2.11 ± 2.06	8.0 ± 7.0	125	8.1	6.3	219	0.20	1.22	0.0029	0.085	1.63	0.74	0.86
V7a	FR	9	37.3	2.11 ± 2.02	10.5 ± 9.5	125	7.7	6.3	199	0.23	1.22	0.0029	0.081	1.41	0.71	
V8a	FR	8	36.8	2.11 ± 2.05	11.5 ± 8.5	125	7.6	6.0	185	0.22	1.19	0.0030	0.079	1.21	0.65	
V9a	FR	8	37.3	2.11 ± 2.03	12.5 ± 7.5	125	7.7	6.0	178	0.23	1.17	0.0029	0.076	2.51	0.58	
V10a	FR	7	38.3	2.12 ± 2.07	15.0 ± 5.0	125	7.9	5.3	162	0.19	1.13	0.0030	0.075	1.42	0.60	
V11a	FR	6	38.3	2.11 ± 2.04	17.5 ± 2.5	125	7.9	5.2	177	0.14	1.15	0.0031	0.076	2.79	0.65	
A1a	FR	14	42.6	2.12 ± 2.03	8.0 ± 7.0	25	8.8	6.5	218	0.25	1.18	0.0026	0.075	2.52	0.80	
A2a	FR	15	45.0	2.12 ± 2.04	8.0 ± 7.0	0.625 ± 0.375	9.3	6.4	234	0.21	1.18	0.0026	0.078	1.54	0.81	
A3a	FR	13	41.6	2.12 ± 2.07	8.0 ± 7.0	50 ± 25	8.6	6.6	219	0.27	1.21	0.0026	0.075	3.09	0.80	
A4a	FR	13	41.6	2.12 ± 2.03	8.0 ± 7.0	62.5 ± 37.5	8.6	6.6	213	0.28	1.17	0.0026	0.074	1.64	0.80	
A5a	FR	14	44.6	2.11 ± 2.07	8.0 ± 7.0	137.5 ± 12.5	9.2	6.4	231	0.23	1.18	0.0026	0.077	1.59	0.86	
A6a	CL	26	40.7	2.49 ± 2.45	4.0 ± 2.0	5	8.4	6.8	262	0.19	1.23	0.0028	0.091	1.55	0.93	
A7a	CL	25	39.2	2.48 ± 2.44	4.0 ± 2.0	10	8.1	7.0	249	0.24	1.21	0.0028	0.087	1.51	0.94	
A8a	CL	25	39.2	2.48 ± 2.44	4.0 ± 2.0	20	8.1	7.1	253	0.24	1.18	0.0028	0.088	1.50	1.00	
S1a	CL	13	41.2	2.11 ± 2.07	8.0 ± 7.0	200	8.5	7.1	270	0.23	1.22	0.0025	0.077	3.27	0.86	
S2a	CL	12	37.3	2.11 ± 2.07	8.0 ± 7.0	200	7.7	6.2	218	0.18	1.19	0.0031	0.090	1.46	0.77	
S3a	CL	9	26.6	2.11 ± 2.07	8.0 ± 7.0	200	5.5	5.6	172	0.14	1.20	0.0042	0.110	1.31	0.68	
S4a	CL	154	37.3	2.11 ± 2.07	0.625 ± 0.375	200	7.7	7.6	280	0.25	1.72	0.0027	0.083	6.36	1.94	
S5a	CL	51	39.2	2.10 ± 2.06	2.0 ± 1.0	200	8.1	7.5	280	0.25	1.29	0.0027	0.090	2.30	1.56	
S6a	CL	35	40.2	2.11 ± 2.07	3.0 ± 2.0	250	8.3	7.2	268	0.23	1.28	0.0028	0.089	1.88	1.08	1.00
S7a	CL	17	40.2	2.10 ± 2.06	6.0 ± 4.0	200	8.3	6.6	237	0.21	1.16	0.0028	0.085	1.39	0.83	
C1a	10CL	12	38.3	2.12 ± 2.08	8.0 ± 7.0	200	7.9	6.5	216	1.57	1.18	0.0028	0.082	2.56	0.79	
C2a	5FR	12	38.3	2.11 ± 2.07	8.0 ± 7.0	200	7.9	6.4	215	0.99	1.18	0.0029	0.082	1.63	0.78	

Continued on next page...

Table A2 – Continued

Case	Mode	Ro	Re_M $\times 10^3$	$T \pm t$ [s]	$\Omega \pm \omega$ [Hz]	$A \pm \alpha$ [Hz/s]	U [m/s]	T_q [%]	Re_λ	$\langle\epsilon\rangle M/U^3$ $\times 10^3$	u'/v'	η/M	λ/M	L_{ux}/M	L_{vx}/M	L_{uy}/M
C3a	6CL	13	38.7	2.14 ± 2.10	8.0 ± 7.0	200	8.0	6.5	223	0.93	1.19	0.0028	0.083	1.62	0.79	
C4a	3FR	13	38.7	2.14 ± 2.10	8.0 ± 7.0	200	8.0	6.5	221	0.86	1.16	0.0028	0.083	1.43	0.87	
C5a	4CL	13	38.7	2.14 ± 2.10	8.0 ± 7.0	200	8.0	6.5	216	1.56	1.20	0.0028	0.082	2.68	0.75	
C6a	2FR	13	38.7	2.14 ± 2.10	8.0 ± 7.0	200	8.0	6.6	229	1.86	1.22	0.0028	0.085	3.46	0.82	
C7a	10CL	51	39.2	2.12 ± 2.08	2.0 ± 1.0	200	8.1	7.7	321	0.82	1.33	0.0027	0.090	2.34	1.46	
C8a	5FR	51	39.2	2.12 ± 2.07	2.0 ± 1.0	200	8.1	7.6	280	0.83	1.35	0.0027	0.089	2.38	1.33	
C9a	6CL	51	39.2	2.16 ± 2.12	2.0 ± 1.0	200	8.1	7.5	274	0.81	1.39	0.0027	0.088	2.32	1.20	
C10a	3FR	51	39.2	2.15 ± 2.11	2.0 ± 1.0	200	8.1	7.6	281	0.84	1.33	0.0027	0.089	2.39	1.39	
C11a	4CL	51	39.2	2.16 ± 2.11	2.0 ± 1.0	200	8.1	7.5	270	0.83	1.31	0.0027	0.088	2.17	1.30	
C12a	2FR	51	39.7	2.14 ± 2.09	2.0 ± 1.0	200	8.2	7.5	285	0.80	1.35	0.0027	0.091	2.36	1.41	
C13a	10CL	33	38.3	2.12 ± 2.08	3.0 ± 2.0	250	7.9	7.2	250	0.76	1.17	0.0028	0.086	1.55	1.28	0.99
G1a	FR	12	38.3	2.12 ± 2.02	8.0 ± 7.0	200	7.9	6.4	214	0.22	1.17	0.0029	0.082	2.15	0.76	
G2a	FR	50	38.7	2.12 ± 2.03	2.0 ± 1.0	200	8.0	7.5	300	0.21	1.36	0.0027	0.088	2.19	1.27	
G3a	CL	13	39.2	2.11 ± 2.07	8.0 ± 7.0	200	8.1	6.6	237	0.22	1.21	0.0028	0.086	3.59	0.73	
G4a	CL	50	38.7	2.11 ± 2.06	2.0 ± 1.0	200	8.0	7.4	267	0.26	1.33	0.0027	0.088	2.11	1.35	
R1a	FR	13	41.2	2.11 ± 2.07	8.0 ± 7.0	250	8.5	6.3	250	0.16	1.26	0.0030	0.092	1.88	0.89	
R2a	FR	53	41.2	2.12 ± 2.07	2.0 ± 1.0	250	8.5	7.1	290	0.19	1.38	0.0028	0.095	2.47	1.34	
R3a	CL	53	40.7	2.10 ± 2.06	2.0 ± 1.0	250	8.4	7.2	329	0.16	1.38	0.0028	0.096	2.49	1.46	

Table A3: Grid and flow properties for test cases with solid square wings. All measurements were performed at $x/M = 30$.

Case	Mode	Ro	Re_M $\times 10^3$	$T \pm t$ [s]	$\Omega \pm \omega$ [Hz]	$A \pm \alpha$ [Hz/s]	U [m/s]	T_q [%]	Re_λ	$\langle\epsilon\rangle M/U^3$ $\times 10^3$	u'/v'	η/M	λ/M	L_{ux}/M	L_{vx}/M	L_{uy}/M
T1b	FR	16	38.3	2.11 ± 2.07	6.0 ± 4.0	125	7.9	8.6	285	0.42	1.19	0.0024	0.079	1.58	0.91	
T4b	FR	18	40.7	3.18 ± 3.14	6.0 ± 4.0	125	8.4	8.2	302	0.33	1.17	0.0024	0.083	1.62	0.94	
T5b	FR	17	38.7	5.40 ± 5.36	6.0 ± 4.0	125	8.0	8.4	283	0.39	1.15	0.0024	0.080	1.45	0.90	
T6b	FR	17	38.7	7.78 ± 2.69	6.0 ± 4.0	125	8.0	8.4	286	0.38	1.13	0.0024	0.081	1.38	0.95	
V1b	FR	160	38.7	2.11 ± 2.02	0.625 ± 0.375	125	8.0	9.6	426	0.30	1.64	0.0024	0.092	6.19	2.92	
V2b	FR	80	38.7	2.11 ± 2.06	1.25 ± 0.75	125	8.0	9.6	423	0.30	1.41	0.0024	0.091	3.30	2.03	
V3b	FR	51	39.7	2.11 ± 2.06	2.0 ± 1.0	125	8.2	9.5	376	0.37	1.24	0.0024	0.092	2.26	1.46	
V4b	FR	33	38.3	2.11 ± 2.07	3.0 ± 2.0	125	7.9	9.6	353	0.42	1.24	0.0024	0.089	3.67	1.31	1.00
V5b	FR	17	38.7	2.11 ± 2.03	5.5 ± 4.5	125	8.0	8.6	303	0.38	1.21	0.0025	0.084	1.81	1.08	0.93
V6b	FR	12	38.3	2.11 ± 2.06	8.0 ± 7.0	125	7.9	8.0	274	0.33	1.23	0.0025	0.083	2.52	0.96	0.89
V7b	FR	10	38.7	2.11 ± 2.02	10.5 ± 9.5	125	8.0	7.7	269	0.30	1.22	0.0026	0.084	1.70	0.90	
V8b	FR	9	38.3	2.11 ± 2.05	11.5 ± 8.5	125	7.9	7.4	250	0.30	1.20	0.0026	0.082	2.69	0.85	
V10b	FR	7	38.3	2.12 ± 2.07	15.0 ± 5.0	125	7.9	6.6	222	0.24	1.20	0.0027	0.081	1.68	0.84	
V11b	FR	6	39.2	2.11 ± 2.04	17.5 ± 2.5	125	8.1	6.3	227	0.20	1.22	0.0028	0.084	1.97	0.86	
A2b	FR	13	39.2	2.12 ± 2.04	8.0 ± 7.0	0.625 ± 0.375	8.1	7.7	276	0.30	1.26	0.0026	0.085	2.60	0.94	
A5b	FR	13	39.2	2.11 ± 2.07	8.0 ± 7.0	137.5 ± 12.5	8.1	7.7	271	0.30	1.22	0.0026	0.083	1.70	0.96	
A6b	CL	25	38.7	2.49 ± 2.45	4.0 ± 2.0	5	8.0	8.6	307	0.37	1.21	0.0025	0.085	1.63	1.04	
A7b	CL	25	39.2	2.48 ± 2.44	4.0 ± 2.0	10	8.1	8.7	316	0.37	1.21	0.0024	0.086	1.68	1.05	
A8b	CL	25	39.2	2.48 ± 2.44	4.0 ± 2.0	20	8.1	8.8	326	0.36	1.19	0.0025	0.087	1.62	1.15	
S5b	CL	51	39.7	2.10 ± 2.06	2.0 ± 1.0	200	8.2	9.3	357	0.38	1.30	0.0024	0.089	2.38	1.48	
S7b	CL	17	39.2	2.10 ± 2.06	6.0 ± 4.0	200	8.1	8.3	297	0.36	1.19	0.0024	0.082	1.67	1.14	
C1b	10CL	13	38.7	2.12 ± 2.08	8.0 ± 7.0	200	8.0	8.2	285	1.51	1.24	0.0025	0.083	3.67	0.85	
C3b	6CL	12	37.3	2.14 ± 2.10	8.0 ± 7.0	200	7.7	8.7	332	1.66	1.27	0.0024	0.082	3.91	0.92	
C5b	4CL	13	38.7	2.14 ± 2.10	8.0 ± 7.0	200	8.0	8.3	294	1.21	1.21	0.0025	0.085	2.90	1.03	

Table A4: Grid and flow properties for test cases with solid circular wings. All measurements were performed at $x/M = 30$.

Case	Mode	Ro	Re_M $\times 10^3$	$T \pm t$ [s]	$\Omega \pm \omega$ [Hz]	$A \pm \alpha$ [Hz/s]	U [m/s]	T_q [%]	Re_λ	$\langle\epsilon\rangle M/U^3$ $\times 10^3$	u'/v'	η/M	λ/M	L_{ux}/M	L_{vx}/M	L_{uy}/M
V1c	FR	168	40.7	2.11 ± 2.02	0.625 ± 0.375	125	8.4	8.0	379	1.19	1.67	0.0027	0.096	6.88	2.51	
V2c	FR	95	46.0	2.11 ± 2.06	1.25 ± 0.75	125	9.5	8.1	406	0.19	1.48	0.0024	0.089	3.80	1.76	
V4c	FR	35	40.2	2.12 ± 2.04	3.0 ± 2.0	250	8.3	7.9	318	0.25	1.23	0.0027	0.093	2.06	1.25	1.03
V6c	FR	13	40.2	2.12 ± 2.07	8.0 ± 7.0	250	8.3	6.9	258	0.22	1.24	0.0028	0.088	2.63	0.82	
S1c	CL	13	40.7	2.11 ± 2.07	8.0 ± 7.0	200	8.4	6.9	262	0.21	1.19	0.0028	0.089	1.72	0.90	
C1c	10CL	13	40.7	2.12 ± 2.08	8.0 ± 7.0	200	8.4	6.8	260	1.03	1.13	0.0028	0.088	2.15	3.46	